https://eprints.gla.ac.uk/269350/

Performance and Flow Characteristics of the Liquid Turbine for Supercritical Compressed Air Energy Storage System

Hongyang Li
E-mail: lihongyang0@126.com
Institute of Engineering Thermophysics, Chinese Academy of Science
University of Chinese Academy of Sciences

Wen Li
E-mail: liwen@iet.cn
Institute of Engineering Thermophysics, Chinese Academy of Sciences
University of Chinese Academy of Sciences

Xuehui Zhang
E-mail: zhangxuehui@iet.cn
Institute of Engineering Thermophysics, Chinese Academy of Sciences

Yangli Zhu
E-mail: zhuyangli@iet.cn
Institute of Engineering Thermophysics, Chinese Academy of Sciences

Zhitao Zuo
E-mail: zuozhitao@iet.cn
Institute of Engineering Thermophysics, Chinese Academy of Sciences

Haisheng Chen[1]
E-mail: chen_hs@mail.etp.ac.cn
Institute of Engineering Thermophysics, Chinese Academy of Science
University of Chinese Academy of Sciences
National Energy Large Scale Physical Energy Storage Technologies R&D Center of Bijie High-tech Industrial Development Zone

Zhibin Yu
E-mail: Zhibin.Yu@glasgow.ac.uk
James Watt School of Engineering, University of Glasgow

Abstract

The liquid turbine can replace throttling valves during the depressurization process of high-pressure liquid or supercritical fluid and improve the system efficiency of many industrial systems.

---

[1] Corresponding author.

1

However, there is no research about studying the internal flow and total pressure loss of liquid turbines, which can affect the turbine performance significantly. In this paper, performance and flow characteristics in a liquid turbine were analyzed for supercritical compressed air energy storage (SC-CAES) systems in the first time. Three typical topology models (C1, C2 and C3) of the tested liquid turbine were simulated and their performances were compared with experimental results. The deviation of the turbine efficiency between C3 and the experiment is less than 2%, while C1 had a constant increment of the turbine efficiency about 15.8% with the experiment. The total pressure loss in each part was evaluated and the flow characteristics in the nozzle and the rotor were analyzed. Nonuniform flow affected the nozzle's total pressure loss significantly, while the rotor's total pressure loss was related to the development of low energy regions. The results obtained in this paper provides guidance for optimizing liquid turbines and improving the turbine performance for various industrial systems with throttling valves installed.

Keywords: Liquid turbine; CFD; Total pressure loss; Various rotational speeds; Supercritical compressed air energy storage system

1 Introduction

The liquid turbine can replace throttle valves in industrial systems to recover the waste energy of a high-pressure liquid or supercritical fluid and mitigate the vaporization in the depressurization process [1]. The liquid turbine is a kind of liquid expanders which have been applied in various industrial systems, such as liquefied natural gas systems [2,3], air separation systems [4,5], trans-critical CO_2 refrigeration systems [6–11] and other refrigeration systems [12–14], supercritical compressed air (SC-CAES) systems [1,15], and so on. The throttling valve equipped between the heat exchanger and the cryogenic tank wastes the work of compressors. Guo et al. [16,17] argued that the efficiency of the SC-CAES system with the liquid turbine could be improved by 10%. The investigation of the liquid turbine's flow characteristics is essential to the design and operation of thermal systems with liquid turbines installed.

Liquid expanders can be classified mainly into two types, including the positive displacement expander [18–20] and the liquid turbine. The positive displacement expander was preliminarily applied in refrigeration systems, but its performance was limited by the friction and internal leakage inside the expander. The liquid turbine was widely used in various systems and mainly included the impulse type [12–14,21,22] and the reaction type [5,23–27]. Elliot [12] studied experimentally the performance of the single-stage and two-stages two-phase turbines with various two-phase fluids, including nitrogen-water, R22 and steam-water. The output power of the single-stage turbine was 9.9 kW for nitrogen-water, 6.34 kW for R22 and 33.9 kW for steam-water, while the output power of the two-stages turbine was 10.57 kW for nitrogen-water and the turbine efficiency was 50.7%. Hays and Brasz used [22] air and water mixture to simulate the refrigerant for testing the performance of an R134a turbine. Cho et al. [13] tested two-phase turbines with one nozzle and 29 blades using R134a and found that the total-to-static efficiency was 15.7% and the specific output power was 0.4 kJ/kg. He et al. [14] measured a Pelton-type turbine with R410a as the working fluid and the maximum isentropic efficiency was 32.8% and the maximum specific recovery work was 2.45 kJ/kg.

The reaction type liquid turbine was designed and tested for liquefied natural gas [2,3], air separation [4,5], refrigeration [24] and geothermal systems [25–27]. Patel and Kimmel [2] presented

the characteristics of the liquid turbine under various working conditions, while Kimmel and Cathery [28] introduced the principles of two-phase turbines. Date et al. [25,29] measured the performance of a radial outflow two-phase turbine with the brine as the inflow and the gas-water as the outflow, which was applied in geothermal systems. The maximum output power was about 1.33 kW and the isentropic efficiency was about 25%. Wang et al. [5] conducted the experiment of a liquid turbine with liquid nitrogen as the working fluid and the maximum shaft power was about 2.2 kW, while Zhang et al. [24] tested another turbine with R22 as the working fluid and the peak output power was about 100W. Li et al. [1] presented experimental performance of the liquid turbine used in SC-CAES under various working conditions, while the output power was 30.44 kW and the efficiency was 75.16% under the designed flow rate.

In recent years, CFD methods were used to predict the performance and study the characteristics of liquid turbines. Zhao et al. [30] predicted the performance and carried out design optimization of the liquid turbine. Li et al. [31] simulated internal flow in the liquid turbine with the annular bend, the nozzle and the rotor, and analyzed the influences of the blade twist angle, the radial gap and the nozzle vane stager angle on the performance of the turbine. Through CFD, characteristics of cavitation in the liquid turbine were investigated numerically. He et al. [32] presented steady and unsteady performance of the liquid turbine and used Zwart-Gerber-Belamri model [33] to simulate the cryogenic cavitation. Song et al. [34–38] developed optimization methods to design the geometry of the liquid turbine and suppress the cavitation. Wang et al. [39] studied the influence of the impeller faring cone on cavitation. Sun et al. [23] added thermal and turbulence effects into the Rayleigh-Plasset model. Li et al. [40,41] presented preliminary design method of liquid turbines for SC-CAES and applied cavitation models to design the annular nozzle used in multistage two-phase turbines. In addition to the cavitation, numerical simulation has also been applied to predict the strength [42], the axial thrust [43] and rotor dynamics [44] of the liquid turbine. Rane and He [45–48] carried out numerical models to simulate the flashing flow in a radial outflow turbine for geothermal systems. Li et al. [26,27] proposed an inverse design for radial outflow two-phase turbines in geothermal systems and presented performance evaluation methods of the turbine based on the numerical simulation.

Based on previous research, it can be found that the liquid turbine can be the replacement of the throttling valve in various systems and CFD methods are useful in studying the cavitation and other performance of the liquid turbine. However, the flow characteristics of the liquid turbine have not been investigated sufficiently. Firstly, total pressure loss of the liquid turbine has not been analyzed. Secondly, the influence of the volute on the nonuniform flow in the nozzle and the rotor has not been studied. Thirdly, influences of various topological models on the deviation between the simulation and the experiment have not been clarified. These characteristics can not only affect the performance of the liquid turbine, but also influence the operation and reliability of the system. Thus, it is essential to present detailed investigation on the internal flow of the liquid turbine.

In this paper, the numerical method is applied to study the internal flow characteristics of the liquid turbine for SC-CAES systems and validated with experimental results. Section 2 describes the experiment and the simulation of the liquid turbine. Section 3 presents the performance of the liquid turbine under various flow rates and rotational speeds. Section 4 discusses the total pressure loss in each part and the flow characteristics in the nozzle and the rotor under various flow rates. The comparison between the simplified simulation, the whole three-dimensional simulation and the experiment and the performance analysis can help to guide the design and optimization of the liquid

turbines.

2 System, experiment and numerical simulation

2.1 The SC-CAES

The flow chart of the SC-CAES is illustrated in Figure 1. During the charging phase, the air is compressed to the supercritical state by the multi-stage compressors, which are driven by the motor and the electrical power. The supercritical air is cooled in the cold storage/heat exchanger and the state of the air is changed from the supercritical state to the liquid state. Then, the high-pressure liquid air is depressurized by the valve and the low-pressure liquid air is stored in the cryogenic storage tank. During the releasing phase, the liquid air is pressurized to the supercritical pressure and pumped into the cold storage/heat exchanger by the cryopump. The high pressure air is heated in the heat storage/heat exchanger and absorbs the heat of compression. Finally, the air is expanded in the multi-stage expanders and produces the shaft power, which is converted into the electrical power by the generator.
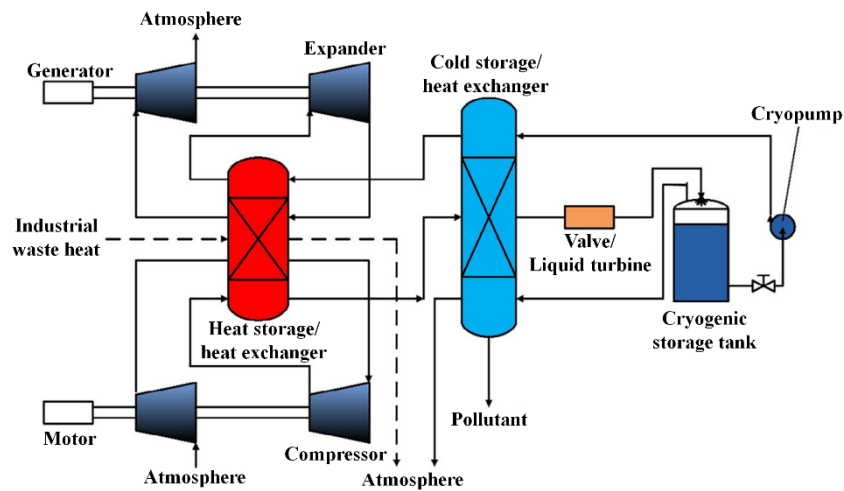
Figure 1 Flow chart of SC-CAES[16]

In the charging process, the pressure of the high-pressure liquid is decreased by the valve. However, both the energy and mass of liquid is wasted in the throttling process. The liquid turbine can replace the valve and recover the energy and liquid. The inlet of the liquid turbine is high-pressure liquid in this study.

2.2 Experiment

The liquid turbine is tested in another cycle, which was described by Li et al[1]. For convenience in testing, a model test method is used and the working fluid in the cycle is water. The model test method for the liquid turbine was proposed by Li et al[41] to simplify the operation conditions of the liquid turbine. The model test method contains two parts. The first part changes the working fluid from the liquid nitrogen to the water and the rotational speed. The second part alters the geometry of the turbine and working conditions. The performance of modelled turbines performance agrees with the prototype if the flow rate is higher than 70% rated flow rate.

As shown in Figure 2(a), the liquid is stored in the liquid tank. The pressure of the liquid is increased by the booster pump to the pressure above the inlet pressure of the liquid turbine. The pressure is stabilized by the buffer vessel. The outflow separates into two ways. The dominated flow rate enters the liquid turbine and is measured by flow meter 1. The other portion of the flow is depressurized by the control valve 1, which can control slightly the flow rate of the liquid turbine.

The outflow of the liquid turbine enters another buffer vessel. The outflow of the buffer vessel separates into two ways. One way is for the circulation pump, which can circulate the major portion of the flow. The other way is for the control valve 2, which can depressurize the flow into the atmospheric pressure. The performance of the liquid turbine is measured by the pressure sensors at the inlet and outlet of the turbine, as well as the torque sensor and the rotational speed sensor. The rotational speed is controlled by the generator and the frequency converter. Figure 2(b) shows the layout of the test section. The turbine has a vertical inlet and a horizontal outlet. The shaft of the turbine is coupled to the shaft of an electrical dynamometer by an elastic coupling. The design rotational speed of the turbine is 1550 rpm. The electrical dynamometer can convert the shaft power of the turbine directly into the electric power and control the rotational speed by a frequency converter. The torque of the turbine is measured by the torque sensor, while the accuracy is ±0.5%. The accuracy of the rotational speed sensor and its accuracy is ±1 rpm.
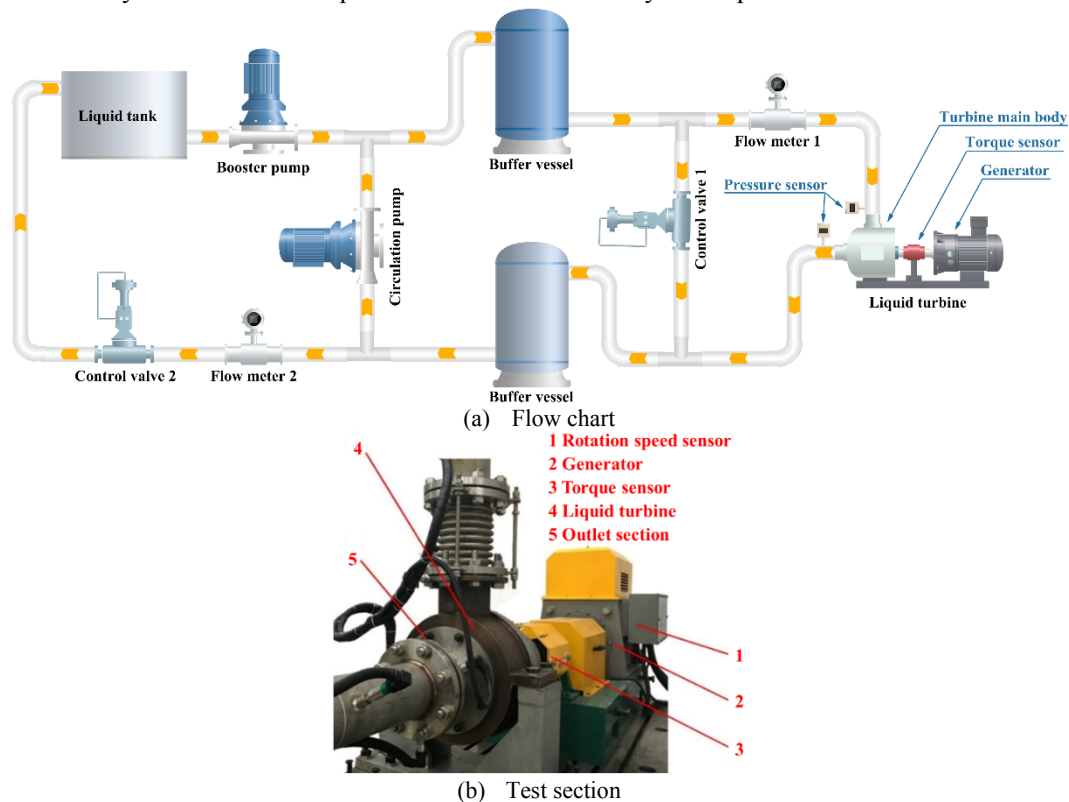

(a) Flow chart

(b) Test section

Figure 2 Flow chart and test section of the experiment

The geometry of the tested liquid turbine is shown in Figure 3(a). The volute (grey part) is a type of collectors for its convenience in manufacturing and assembling. The nozzle (green part) has 25 blades and is covered by a nozzle plate (purple part). The rotor (gold part) has 19 blades and is installed on the inner side of the nozzle and the nozzle plate. The outlet section (brown part) is connected at the outlet of the rotor for convenience in the measurement. As shown in Figure 3(b), the flow passages in the turbine include the volute, nozzle, rotor, interspace, Gap A, Gap B and outlet. The dominated liquid flows from the volute, enters the nozzle and rotates the rotor. However, there is also a fraction of flow leaking into Gap A and Gap B. The flow in Gap A not only produces frictional power on the front plate, but also generates leakage loss through Seal A. The flow in Gap B only produces frictional power on the backplate of the rotor, because the leakage through seal B is blocked by the mechanical seal in the manufacture turbine. The detailed geometry of the liquid turbine is listed in Table 1. The design inlet pressure is 1.4 MPa and the design outlet pressure is
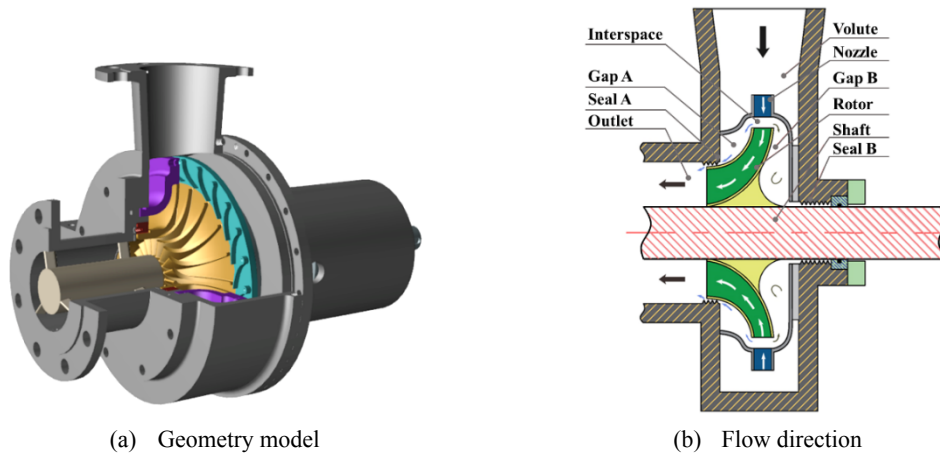
0.7 MPa.

(a) Geometry model   (b) Flow direction

Figure 3 Model of the tested liquid turbine

Table 1 Configuration of the liquid turbine

Parameters	Values
Inlet diameter of the nozzle	405.5 mm
Outlet diameter of the nozzle	319.0 mm
Inlet diameter of the rotor	308.9 mm
Inlet height of the rotor's blade	9.6 mm
Outlet diameter of the rotor's hub	72.9 mm
Outlet diameter of the rotor's shroud	133.7 mm

2.3 Numerical simulation

2.3.1 Simulation configuration

In this paper, three regular kinds of computation domains are studied based on the structure of the manufactured liquid turbine. The first one includes only the nozzle and the rotor and is used to obtain the performance of the nozzle and the rotor. The second one includes the nozzle, the rotor and the volute and can reflect the nonuniform flow caused by the volute and the performance of the volute. The third one includes the whole flow passages in the turbine and can reflect not only the performance of the nozzle, the rotor and the volute, but also the leakage through the seal and the friction loss of the plate. Therefore, three geometrical models are constructed for the tested liquid turbine: the single nozzle and rotor (C1); the volute and all nozzles and rotors (C2); the volute, all nozzles and rotors, Gap A, Gap B and outlet section (C3), as shown in Figure 4(a), (b) and (c).
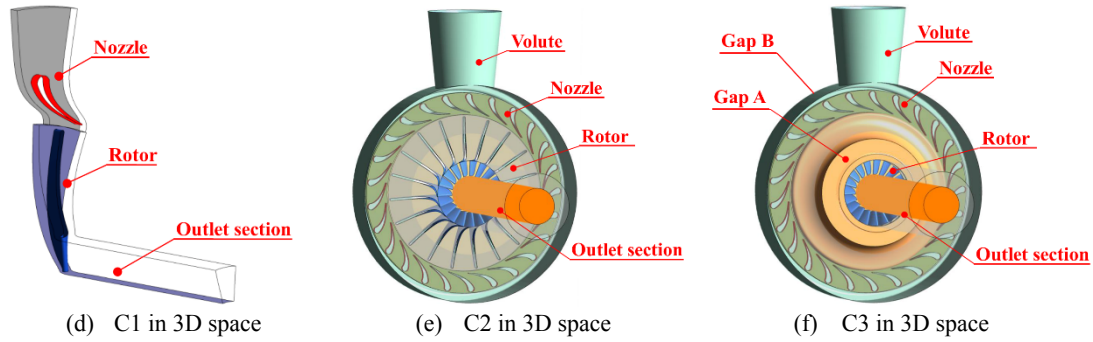

(a) C1 on the meridional plane   (b) C2 on the meridional plane   (c) C3 on the meridional plane

(d) C1 in 3D space   (e) C2 in 3D space   (f) C3 in 3D space
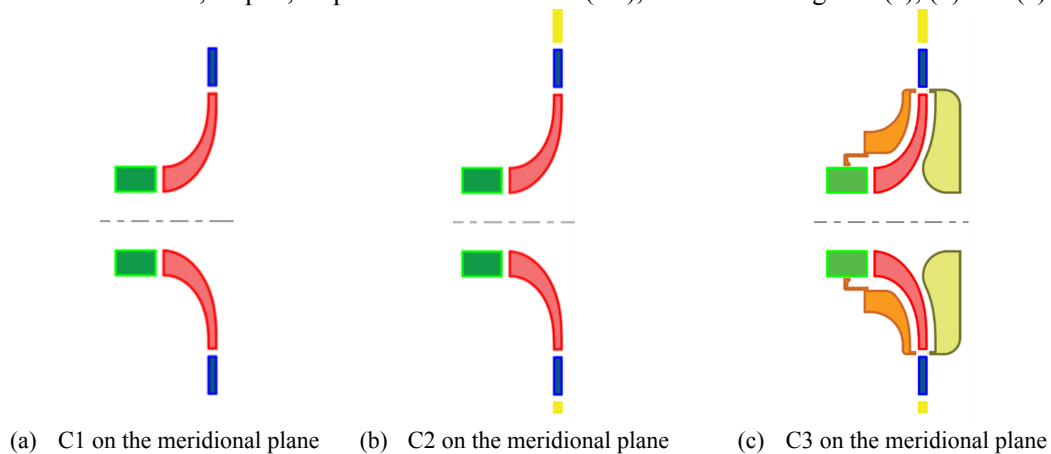
Figure 4 Diagram of geometry models [15]

The corresponding 3D models are built as shown in Figure 4(d), (e) and (f). It should be noted that a small computational domain for the interspace (clearance) is placed between the nozzle and the rotor in C3. The inflow of the interspace comes from the outlet of the nozzle. Three are three outlet boundaries, connecting the rotor, Gap A and Gap B.

The mesh of the nozzle and the rotor is structured and constructed in TurboGrid. The mesh of the outlet section, Gap A and Gap B is also structured and generated in ICEM. The mesh of the volute is unstructured and constructed in ICEM. The mesh sizes of the three models are different and listed in Table 2. ANSYS CFX is used in the paper to simulate the flow in the turbine and evaluate the turbine performance. The mass flow rate is given at the inlet boundary while the pressure is given at the outlet boundary. The turbulence model is k-ε model. The rotor's interfaces are connected to the nozzle and outlet section using the stage (mixing plane) method because the stage method can reflect the total performance of the turbine during operation.

Table 2 Mesh size of the domain in different cases (Unit: Million)

	Volute	Nozzle	Interspace	Rotor	Gap A	Gap B	Outlet	Total
C1	-	1.0	-	0.5	-	-	0.7	2.2
C2	8.6	8.9	-	8.0	-	-	6.1	31.6
C3	8.6	9.2	2.4	8.9	5.4	4.5	4.0	42.9

2.3.2 Mesh independence

Before giving the simulation results of the turbine, the inaccuracy brought by the mesh size is studied by comparing the performance of C1, which has different numbers of elements. The mesh of the nozzle and rotor is illustrated in Figure 5.
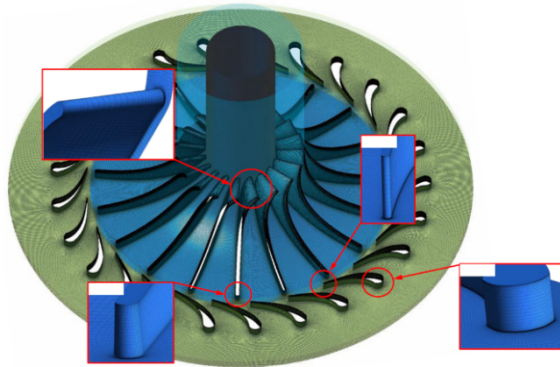

Figure 5 Mesh of the nozzle and rotor

The turbine efficiency is defined as

$$\eta = \frac{W}{(P_{in} - P_{out})Q} \times 100\% \qquad (1)$$

where the numerator represents the real output power of the liquid turbine and the denominator means the ideal output power of the liquid turbine. The mesh of different element numbers ranging from 0.04 million to 2 million has been created. The turbine efficiency deviates from each other if the element number is lower than 1 million, as shown in Figure 6. However, when the element is higher than 1 million, the efficiency keeps about 89.8%. Thus, 1 million element number is sufficient for the simulation of the turbine.
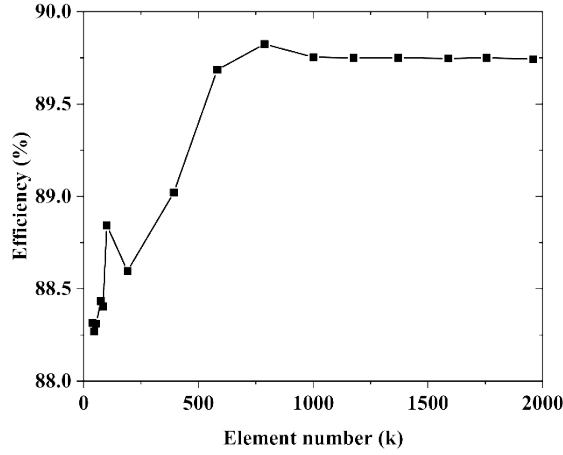

Figure 6 The efficiency of the turbine with different element numbers

3 Results of the experiment and numerical simulation

3.1 Design rotational speed

Among the three models, one of the most differences in the performance results is the turbine efficiency, which can be defined as the ratio between the shaft power and the ideal output energy. The efficiency of the experiment and predicted C1, C2 and C3 at the design rotational speed is illustrated in Figure 6. The predicted and experimental data are fitted using the second-order Gaussian equation in MATLAB, which read as

$$\eta' = a_1 e^{-\left(\frac{Q-b_1}{c_1}\right)^2} + a_2 e^{-\left(\frac{Q-b_2}{c_2}\right)^2} \qquad (2)$$

where η' is the turbine efficiency and the coefficients a_1, b_1, c_1, a_2, b_2 c_2 are listed in Table 3.

Table 3 Coefficients in the fitting equation for the efficiency

	a_1	b_1	c_1	a_2	b_2	c_2
Experiment	73.27	70.08	46.41	15.56	39.93	19.15
C1	54.88	40.74	28.41	84.84	87.98	43.36
C2	54.38	74.19	44.80	43.67	40.87	34.79
C3	73.54	66.08	45.22	10.13	41.36	15.20

As shown in Figure 6, C3 agrees well with the experiment in the entire range of the flow rate and the deviation of the efficiency between C3 and the experiment is less than 2%. The efficiency deviation is the absolute reduction of the efficiency. The low efficiency deviation indicates that the mathematical models, including the turbulence model, interface method and so on, can predict the internal flow in the turbine with high accuracy. Both C1 and C2 have a large deviation from the experiment. At the design flow rate 61 kg/s, the efficiency of the experiment, C1, C2 and C3 is

75.2%, 90.6%, 79.4% and 74.3%, respectively. At the 50% flow rate, the efficiency of the experiment, C1, C2 and C3 is 48.0%, 64.0%, 61.3% and 46.1%, respectively. When the flow rate is lower than the design flow rate, the turbine efficiency of the experiment, C1 and C3 increases with the flow rate. C1's efficiency is higher than the experiment and the deviation of the efficiency $\Delta\eta$ between C1 and the experiment is 15.8% within the entire range of the flow rate. The deviation is caused by the neglect of the nonuniform flow in the volute, the friction loss in the volute and on the front and back plates of the rotor, and the leakage loss through the seal. At the 50% flow rate, the deviation of the efficiency between C2 and the experiment is 13.2%. As the flow rate increases, the deviation decreases. At the 110% flow rate, the deviation of the efficiency between C2 and the experiment is 2.4%. The difference in the efficiency between C1 and C2 increases with the flow rate. At the 50% flow rate, the difference in the efficiency between C1 and C2 is 2.8%, while the difference is 12.8% at the 110% flow rate. The maximum efficiency point of C2 is at 90% of the design flow rate, while the maximum efficiency point of the experiment, C1 and C3 is at 100% of the design flow rate.
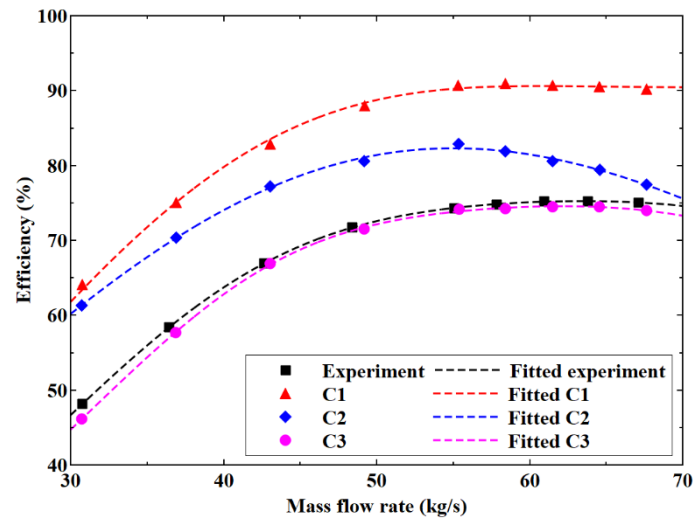

Figure 6 Comparison between efficiencies from the simulation and the experiment

3.2 Various rotational speeds

The efficiency of C1 under various rotational speeds is predicted by using the CFD method and illustrated in Figure 7(a). The predicted efficiency data is fitted using Equation (2). Figure 7(a) indicates that there is a range of flow rate where the efficiency reaches the maximum and the range increases with the rotational speed. The flow rate where the maximum efficiency reaches increases with the rotational speed. The maximum efficiency under various rotational speeds varies between 89.7% and 90.9%.

Table 4 Coefficients in the fitting equation for the C1's efficiency under various rotational speeds

Rotational speed	a_1	b_1	c_1	a_2	b_2	c_2
620 rpm	36.25	20.11	34.60	58.85	51.85	94.55
775 rpm	17.18	32.75	25.91	73.64	42.88	103.8
930 rpm	43.20	29.40	30.99	71.12	74.82	63.38
1085 rpm	45.42	33.25	30.52	75.43	80.20	58.32
1240 rpm	32.59	35.82	24.91	83.65	76.90	58.56
1395 rpm	33.75	37.90	24.25	86.42	80.01	54.91
1550 rpm	54.88	40.74	28.41	84.84	87.98	43.36

|						
1705 rpm	53.65	45.12	30.52	87.00	98.56	50.05

As shown in Figure 6, the C3's efficiency agrees with the experiment better than the C1's efficiency at the design rotational speed. It implies that the accuracy of using the C3 model may be still high under various rotational speeds. However, the mesh size of C3 is much larger than that of C1 and the simulation of C3 costs much longer computational time than C1. Thus, in this paper, a modified prediction method using C1 is used. At the design flow rate, the deviation of the efficiency between C1 and the experiment remains almost the constant value $\Delta\eta$ (in this paper, $\Delta\eta$ is 15.8% obtained by Figure 6 and Figure 7(a)). The C1's efficiency could be modified under various speeds using Equation (3). The experimental data of the turbine efficiency under various rotational speeds is illustrated in Figure 7(b). It can be found that using Equation (3) the modified C1's efficiency agrees with the experiment.

$$\Delta\eta = \eta' - \eta'' \tag{3}$$

where η' is the predicted C1's efficiency, η'' is the experimental C3's efficiency, and $\Delta\eta$ is the efficiency reduction between the predicted C1's efficiency and the experimental C3's efficiency.
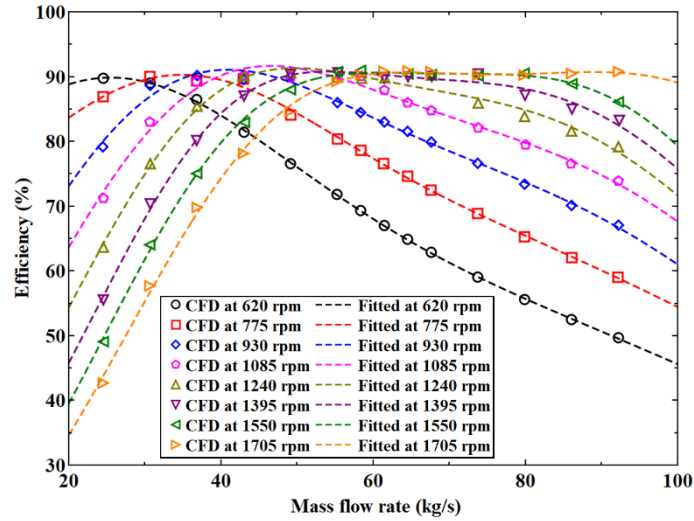
(a) Predicted C1's efficiency
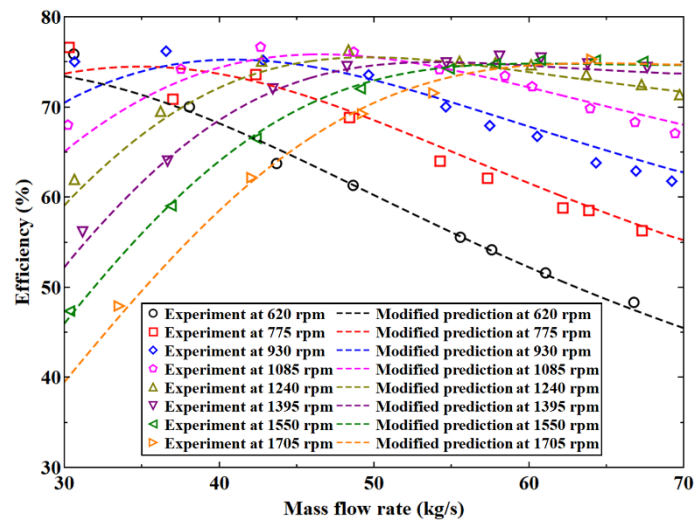
(b) The efficiency of the experiment and modified C1's prediction

Figure 7 Efficiency of the experiment, predicted C1's efficiency and modified C1's prediction

4 Discussion

4.1 Total pressure loss

In the typical turbomachinery, there are several kinds of flow losses including the profile loss, secondary loss, annulus loss and so on [49,50]. Empirical loss expressions have been built for conventional turbines in the previous research [49,51]. Entropy analysis is another method to characterize reflect the energy loss in the turbine [52]. In this paper, because the whole flow details in the turbine are obtained using the simulation. Thus, the relative total pressure loss of each component can be directed calculated as

$$\xi^i = \frac{F_{in}^i - F_{out}^i - W_{ex}^i}{F_{in}^0 - F_{out}^0} \times 100\% \tag{4}$$

The numerator in Equation (4) represents the net energy reduction in the component i. The energy flux F is defined as

$$F^i = P^i Q^i \tag{5}$$

where P is the total pressure and Q is the volumetric flow rate. Using Equation (4), total pressure loss of each C3's component can be derived. The relationship between each part in C3's model and the tested turbine is illustrated in Figure 8(a). The inflow of the liquid turbine enters the volute and the nozzle. The outflow of the nozzle flows into the interspace (clearance) between the nozzle and the rotor, which exists in the assembled liquid turbine. There is flow loss in the interspace caused by the mixing process of the nozzle's outflow due to the trailing flow at the outlet of the nozzle. The major portion of the interspace's outflow enters the rotor, while the others go into Gap A and Gap B. The outlet of Gap A connects to the outlet section, while Gap B is a closed chamber. The rotating walls of Gap A are the front plate of the rotor, while the rotating walls of Gap B are the backplate of the rotor.
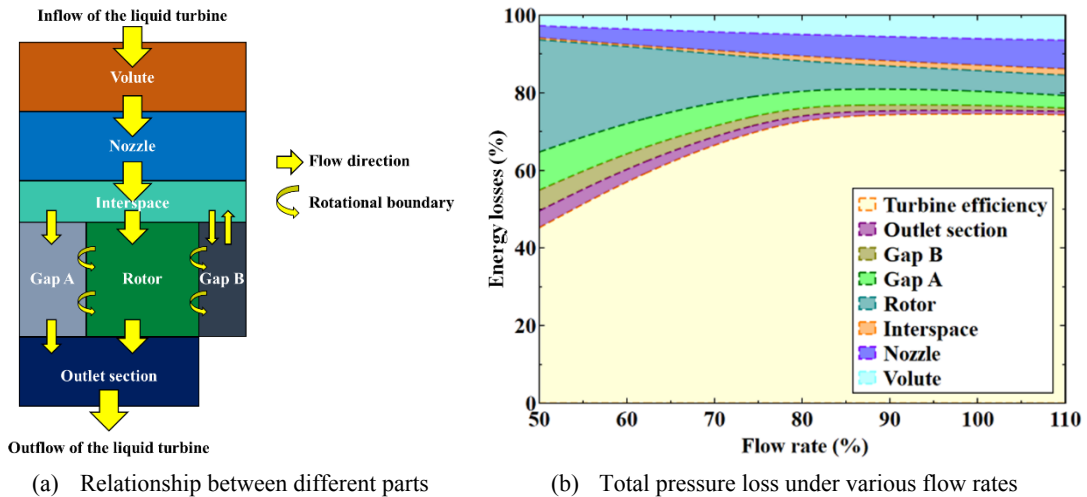
(a) Relationship between different parts   (b) Total pressure loss under various flow rates

Figure 8 Relationship between different parts and total pressure loss at the design rotational speed

As shown in Figure 8(b), at the design flow rate (100% flow rate), the relative total pressure loss of the volute, nozzle, interspace, rotor, Gap A, Gap B and outlet section is 6.1%, 6.8%, 1.4%, 5.5%, 3.7%, 1.3% and 0.9%, respectively. The flow loss of the nozzle accounts for the largest proportion among all parts at the 100% flow rate. In addition to the nozzle's flow loss, the relative total pressure loss of the volute and the rotor are larger than 5%. Gap A's flow loss is mainly caused

by leakage. At 50% flow rate, the relative total pressure loss of the volute, nozzle, interspace, rotor, Gap A, Gap B and outlet section is 2.7%, 3.2%, 0.5%, 28.9%, 9.8%, 5.3% and 4.3%, respectively. The rotor's relative total pressure loss accounts for the largest proportion among all parts at the 50% flow rate. Gap A's relative total pressure loss accounts for the second-largest proportion and is caused by the increment of the ratio between the leakage flow rate and the total flow rate. The Gap B's relative total pressure loss is also larger than 5%. The rotor's relative total pressure loss increases significantly as the flow rate decreases due to the increment of the incidence loss. Total pressure loss of the nozzle and the volute decrease with the flow rate due to the reduction of the flow velocity. Total pressure loss of Gap A and outlet section increase slightly as the flow rate decreases. Within the entire range of the flow rate, the volute's flow loss varies between 2.7% and 6.4%, the nozzle's flow rate varies between 3.2% and 7.4%, and the rotor's relative total pressure loss varies between 5.2% and 28.9%. Gap B's relative total pressure loss varies between 0.8% and 5.3%, while Gap A's relative total pressure loss varies between 3.3% and 9.8%. The outlet section's relative total pressure loss varies between 0.9% and 4.3% and the interspace's relative total pressure loss varies between 0.5% and 1.6%.

4.2 Flow characteristics

4.2.1 Nozzle

The geometry of the volute is not axisymmetric, because there is an inlet port connected to the inner wall of the volute, as shown in Figure 2(a), Figure 3(b) and Figure 4(f). The energy flux at each channel of the nozzle is calculated to characterize the uniform flow. The individual passage of the nozzle is covered by several surfaces, including the inlet, outlet, hub, shroud, the pressure side and the suction side, as shown in Figure 9(a).

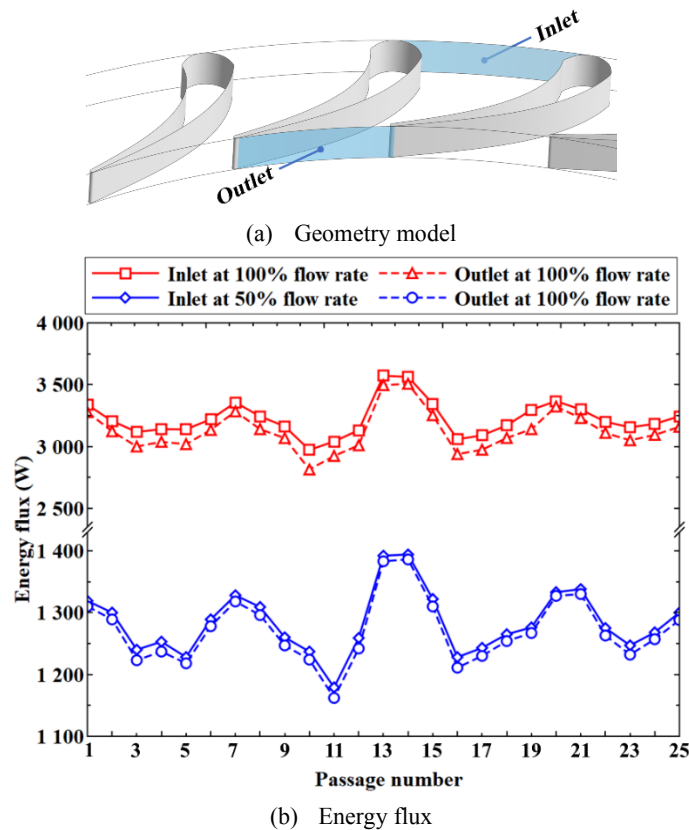(a)　Geometry model

(b)　Energy flux

Figure 9 Energy flux in the nozzle

The energy flux at the inlet can reflect the nonuniform flow rate and pressure distribution

caused by the volute. The energy flux in the individual passage of the nozzle is illustrated in Figure 9(b). The energy flux at the inlet is different in each passage. Passage 13 and 14 face the inlet portion of the volute, so the energy flux in the two passages is much higher than that in the other passages. The fluctuation of the energy flux shows that the position of the inlet position significantly affects the flow in the nozzle. At the 50% flow rate, the fluctuation of the energy flux is similar to that at the 100% flow rate.

4.2.2 Rotor

The increment of the rotor's relative total pressure loss with the reduction of the flow rate is the largest compared with other components. The increment is caused by the incidence loss and the intensification of the inlet vortex. Figure 10 shows contours of the relative velocity under various flow rates at the design rotational speed on the blade to blade view. Because the liquid turbine is designed with a negative incidence angle at the inlet of the rotor, a low-velocity region (S1) exists near the pressure side of the blade. S1 extends from the pressure side towards the suction side and streamwise towards the outlet as the flow rate decreases. At the 80% flow rate, S1 accounts for about 50% of the passage's area. At the 70% flow rate, there is another low-velocity region (S2) in the middle of the downstream passage. At the 60% flow rate, S2 extends streamwise and attaches to the suction side of the blade. At the 50% flow rate, S1 and S2 connect and the relative velocity near the front of the suction side increases. It can be found that S1 is generated at the front of the pressure side, but does not attach to the suction side, while S2 generates in the middle of the passage and attaches to the suction side but does not attach to the pressure side.

(a) 100% flow rate

(b) 90% flow rate

(c) 80% flow rate

(d) 70% flow rate
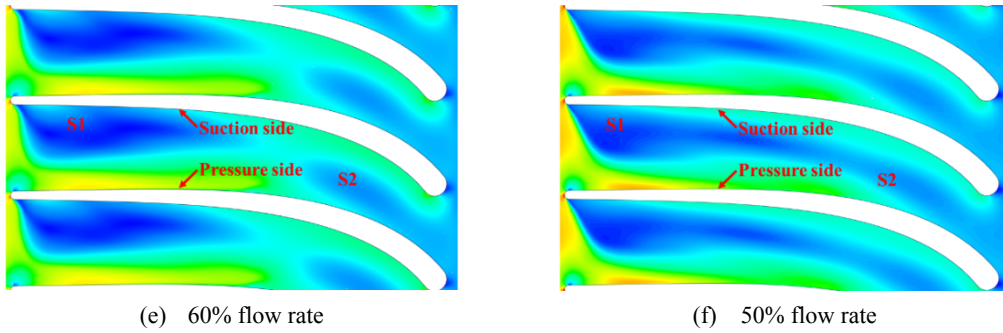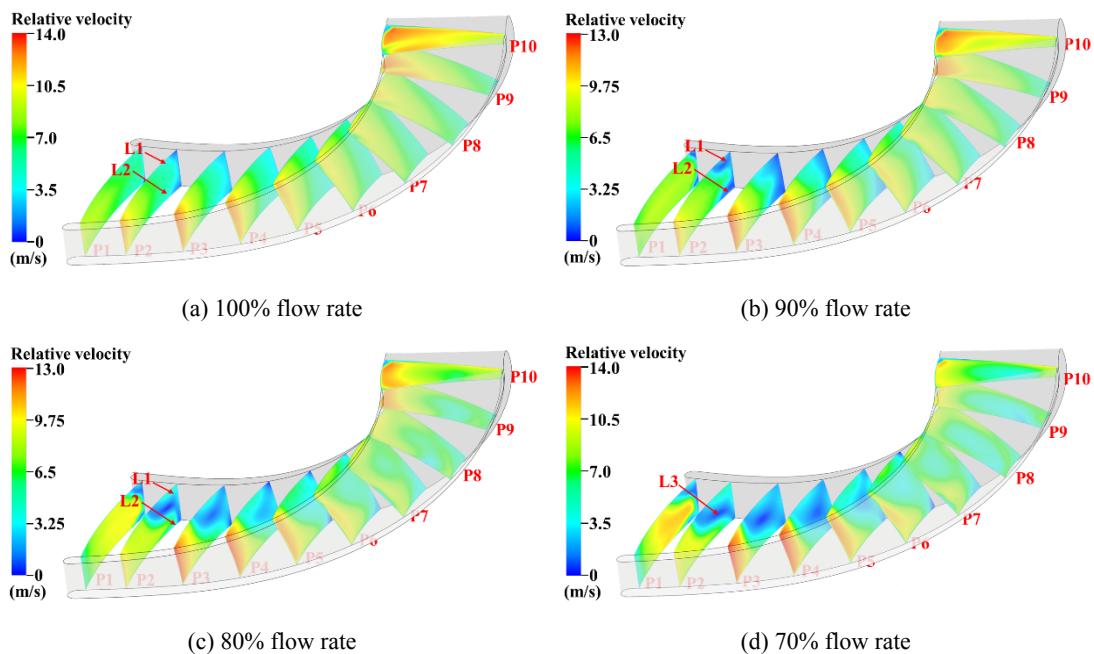
(e) 60% flow rate   (f) 50% flow rate
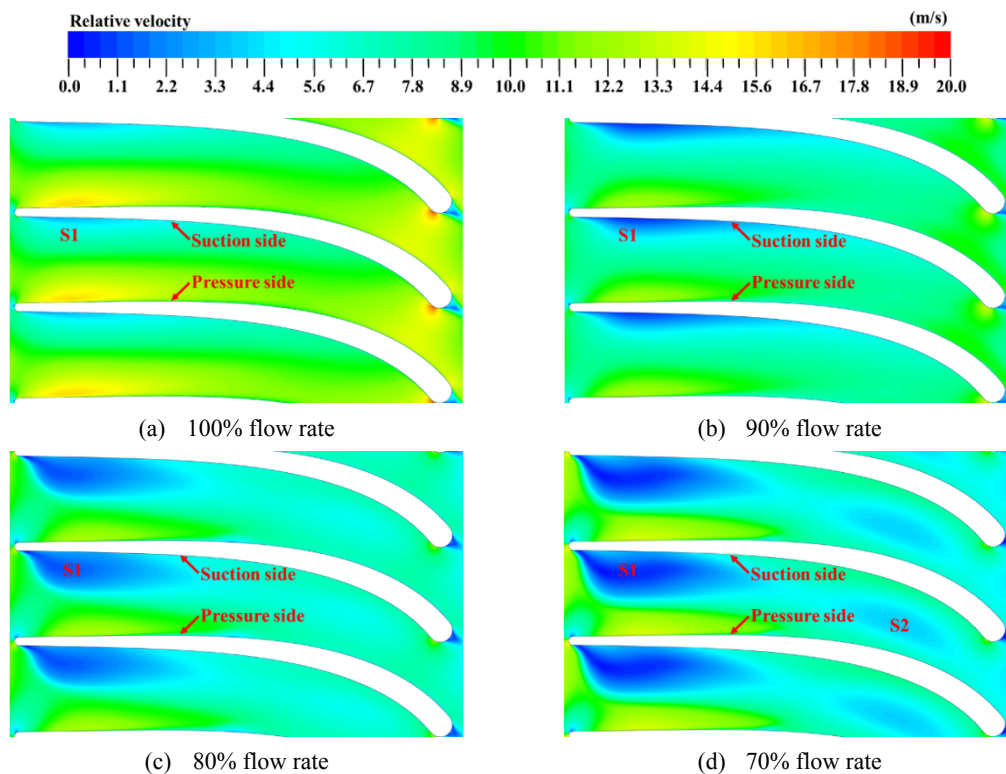
Figure 10 Contours of relative velocity on the mid-span plane at 100% rotational speed

Figure 11 shows contours of the relative velocity on ten planes along the streamwise direction and can illustrate the development of the low-velocity region. The planes are distributed uniformly from the front to the end of the rotor's passage. The low-velocity region S1 in Figure 10(a) is larger near the corners (L1 and L2) of the shroud and the hub, as shown in Figure 11(a). At the 100% flow rate, the size of L1 is almost equal to that of L2. On P2, sizes of L1 and L2 are the largest and decrease along the streamwise direction. As the flow rate decreases, sizes of L1 and L2 increase. At the 90% flow rate, L1 is slightly larger than L2 on P2. At the 80% flow rate, L1 increases significantly and extends towards L2 apparently on P3, P4 and P5. At the 70% flow rate, the low-velocity region L3 is the integrated and further developed region of L1 and L2. L3 extends along the streamwise direction and becomes the largest on P3. The size of L3 on P3 at the 70% flow rate is larger than that on the 80% flow rate. At the 60% flow rate, the size of L3 reaches the largest on P4 and the low-velocity region S2 becomes obvious on P9 and P10. At the 50% flow rate, the velocity near the shroud and the hub is higher than the middle of the passage on P4. The low-velocity core develops along the streamwise direction. It can be found that the wall effect of the shroud significantly affects the development of the low-velocity region.
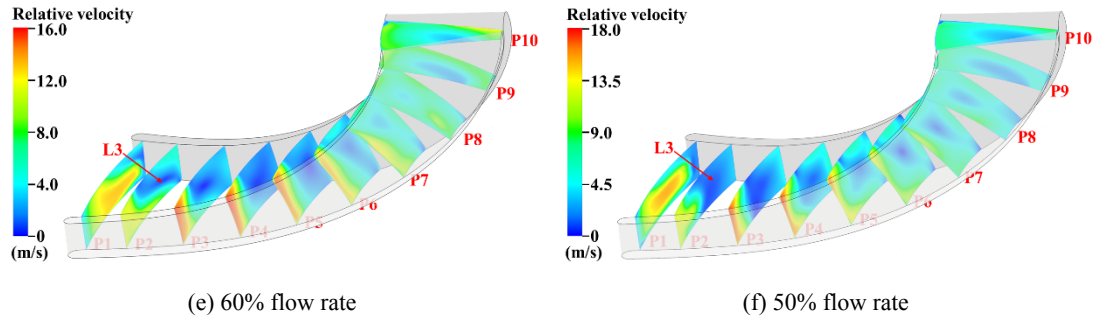

(a) 100% flow rate   (b) 90% flow rate

(c) 80% flow rate   (d) 70% flow rate

<div style="text-align:center">(e) 60% flow rate   (f) 50% flow rate</div>

Figure 11 Contours of relative velocity on various streamwise planes

5 Conclusion

The liquid turbine is an energy recovery device, which is a desirable replacement of the throttling valve during the depressurization process in industrial systems. In this paper, the performance and flow characteristics of the liquid turbine are analyzed based on experimental and numerical results. Detailed conclusions include:

(1) The predicted performance of three computational domains (C1, C2 and C3) is compared with the experimental results. The C3's efficiency agrees with the experiment and the deviation between C3 and the experiment is less than 2%.

(2) C1 has a constant deviation (about 15.8%) from the experiment at the design rotational speed under various flow rates. Using the constant deviation, the modified predicted performance of C1 agrees well with the experimental results under various rotational speeds.

(3) As the flow rate decreases, the rotor's relative total pressure loss increases due to the increment of the incidence loss in the rotor's passage, while the nozzle's relative total pressure loss decreases due to the reduction of the velocity.

(4) The geometry of the velocity affects significantly the nonuniform flow in the nozzle. The position of the inlet portion intensifies the energy flux. Under various flow rates, the energy flux distribution in individual nozzle's passage is similar, although the magnitude of the energy flux decreases with the flow rate.

(5) The low-velocity regions develop in three-dimensional directions. The low-velocity region starts from the suction side near the shroud and the hub. As the flow rate decrease, the wall effect of the shroud becomes more and more significant along the streamwise direction.

The unsteady flow in the turbine will be studied in the future research through using frozen rotor method and experimental data. The geometry of the nozzle and volute will be also optimized in the future research.

Acknowledgement

Nomenclature

Variables

<div style="text-align:center">15</div>

F	Energy flux, W
Q	Volume flow rate, m³/s
p	Pressure, Pa
Δp	Pressure difference, Pa
P	Total pressure, Pa
W	Power, W
Greek symbols	
η	Efficiency, %
ρ	Density, kg/m³
ξ	The relative total pressure loss, %
Superscripts	
0	The whole turbine
i	Component number
Subscripts	
ex	Output
in	Inlet
out	Outlet

Author Contributions

H.L. mainly contributes in the methodology, investigation, experiment, CFD, flow analysis and original draft preparation; W.L. mainly contributes in the methodology, experiment, flow analysis and draft review and editing; X.Z. mainly contributes in the methodology and experiment; Y.Z. mainly contributes in the methodology; Z.Z. mainly contributes in the experiment; H.C. mainly contributes in the draft review and editing, project administration and funding acquisition; Z.Y. mainly contributes in the flow analysis and draft review. All authors have read and agreed to the published version of the manuscript.

Conflicts of Interest

The authors declare that they have no known competing financial interests or personal relationships that could have appeared to influence the work reported in this paper.

References

[1]   H. Li, X. Zhang, W. Li, Y. Zhu, Z. Zuo, H. Chen, Experimental investigation of a liquid turbine in a full performance test rig, Proc. Inst. Mech. Eng. Part A J. Power Energy. 233 (2018) 337–345. https://doi.org/10.1177/0957650918785793.

[2]   V.P. Patel, H.E. Kimmel, Fifteen years of field experience in LNG expander technology, in: Proc. First Middle East Turbomach. Symp., Doha, Qatar, 2011: pp. 7–18. https://doi.org/10.21423/R1HK96.

[3]   M.L. Cords, Multistage liquefied gas expander with variable geometry hydraulic stages, US8497616B2, 2011.

[4]   S. Sgambati, F. Haensel, Cryogenic liquid expansion turbine, WO2013057561A1, 2011.

[5]   K. Wang, J. Sun, P. Song, Experimental study of cryogenic liquid turbine expander with

closed-loop liquefied nitrogen system, Cryogenics (Guildf). 67 (2015) 4–14. https://doi.org/10.1016/j.cryogenics.2015.01.004.

[6]   B. Zhang, X. Peng, Z. He, Z. Xing, P. Shu, Development of a double acting free piston expander for power recovery in transcritical CO2 cycle, Appl. Therm. Eng. 27 (2007) 1629–1636. https://doi.org/10.1016/j.applthermaleng.2006.05.034.

[7]   H.J. Kim, J.M. Ahn, S.O. Cho, K.R. Cho, Numerical simulation on scroll expander-compressor unit for CO2 trans-critical cycles, Appl. Therm. Eng. 28 (2008) 1654–1661. https://doi.org/10.1016/j.applthermaleng.2007.11.002.

[8]   M. Fukuta, T. Yanagisawa, M. Higashiyama, Y. Ogi, Performance of vane-type CO2 expander and characteristics of transcritical expansion process, HVAC&R Res. 15 (2009) 711–727. https://doi.org/10.1080/10789669.2009.10390859.

[9]   B. Yang, X. Peng, Z. He, B. Guo, Z. Xing, Experimental investigation on the internal working process of a CO2 rotary vane expander, Appl. Therm. Eng. 29 (2009) 2289–2296. https://doi.org/10.1016/j.applthermaleng.2008.11.023.

[10]   X. Jia, B. Zhang, L. Pu, B. Guo, X. Peng, Improved rotary vane expander for trans-critical CO2 cycle by introducing high-pressure gas into the vane slots, Int. J. Refrig. 34 (2011) 732–741. https://doi.org/10.1016/j.ijrefrig.2010.12.005.

[11]   M. Karampour, S. Sawalha, State-of-the-art integrated CO2 refrigeration system for supermarkets: A comparative analysis, Int. J. Refrig. 86 (2018) 239–257. https://doi.org/10.1016/J.IJREFRIG.2017.11.006.

[12]   D.G. Elliot, Theory and tests of two-phase turbines, Pasadena, California, US, 1982. https://doi.org/10.2172/5346135.

[13]   S.-Y. Cho, C.-H. Cho, C. Kim, Performance characteristics of a turbo expander substituted for expansion valve on air-conditioner, Exp. Therm. Fluid Sci. 32 (2008) 1655–1665. https://doi.org/10.1016/j.expthermflusci.2008.05.007.

[14]   T. He, C. Xia, Y. Zhao, L. Li, P. Shu, An experimental study on energy recovery by a pelton-type expander in a domestic refrigeration system, HVAC&R Res. 15 (2009) 785–799. https://doi.org/10.1080/10789669.2009.10390864.

[15]   H. Li, Experimental and numerical invesitgation of liquid expanders, University of Chinese Academy of Sciences, 2018.

[16]   H. Guo, Y. Xu, H. Chen, X. Zhou, Thermodynamic characteristics of a novel supercritical compressed air energy storage system, Energy Convers. Manag. 115 (2016) 167–177. https://doi.org/10.1016/j.enconman.2016.01.051.

[17]   H. Guo, Y. Xu, H. Chen, C. Guo, W. Qin, Thermodynamic analytical solution and exergy analysis for supercritical compressed air energy storage system, Appl. Energy. 199 (2017) 96–106. https://doi.org/10.1016/j.apenergy.2017.04.068.

[18]   O. Dumont, R. Dickes, V. Lemort, Experimental investigation of four volumetric expanders, Energy Procedia. 129 (2017) 859–866. https://doi.org/10.1016/j.egypro.2017.09.206.

[19]   M. Kakuda, H. Nagata, F. Ishizono, Development of a scroll expander for the CO2 refrigeration cycle, HVAC&R Res. 15 (2009) 771–783. https://doi.org/10.1080/10789669.2009.10390863.

[20]   G. Galoppi, R. Secchi, L. Ferrari, G. Ferrara, S. Karellas, D. Fiaschi, Radial piston expander as a throttling valve in a heat pump: Focus on the 2-phase expansion, Int. J. Refrig. 82 (2017) 273–282. https://doi.org/10.1016/j.ijrefrig.2017.06.025.

[21] W.J. Comfort III, C.W. Beadle, Design considerations for a two-phase turbine, in: Symp. Polyph. Flow Turbomachinery, ASME Winter Annu. Meet., San Francisco, California, 1978.

[22] L.G. Hays, J.J. Brasz, Two-phase-flow turbines as stand-alone throttle replacement units in large 2000-5000 ton centrifugal chiller installations, in: Proc. 1998 Int. Compress. Eng. Conf. Purdue, Purdue University, West Lafayette, IN, United States, 1998: pp. 792–802.

[23] S. Sun, J. Sun, W. Sun, P. Song, Enhancing cryogenic cavitation prediction through incorporating modified cavitation and turbulence models, J. Fluids Eng. 143 (2021) 061404. https://doi.org/10.1115/1.4050056.

[24] Z. Zhang, M. Li, Y. Ma, X. Gong, Experimental investigation on a turbo expander substituted for throttle valve in the subcritical refrigeration system, Energy. 79 (2015) 195–202. https://doi.org/10.1016/j.energy.2014.11.007.

[25] A. Date, S. Vahaji, J. Andrews, A. Akbarzadeh, Experimental performance of a rotating two-phase reaction turbine, Appl. Therm. Eng. 76 (2015) 475–483. https://doi.org/10.1016/j.applthermaleng.2014.11.039.

[26] H. Li, S. Rane, Z. Yu, G. Yu, An inverse mean-line design method for optimizing radial outflow two-phase turbines in geothermal systems, Renew. Energy. 168 (2021) 463–490. https://doi.org/10.1016/j.renene.2020.12.079.

[27] H. Li, S. Rane, Z. Yu, Investigation of the performance and flow characteristics of two-phase reaction turbines in total flow geothermal systems, Renew. Energy. 175 (2021) 345–372. https://doi.org/10.1016/j.renene.2021.05.022.

[28] H.E. Kimmel, S. Cathery, Thermo-fluid dynamics and design of liquid-vapour two-phase LNG expanders, in: Proc. GPA Eur. Tech. Meet. Adv. Process Equip., Paris, France, 2010.

[29] A. Date, A. Khaghani, J. Andrews, A. Akbarzadeh, Performance of a rotating two-phase turbine for combined power generation and desalination, Appl. Therm. Eng. 76 (2015) 9–17. https://doi.org/10.1016/j.applthermaleng.2014.08.074.

[30] W. Zhao, J. Sun, H. Zhu, C. Li, G. Cai, G. Ma, Numerical investigation of a cryogenic liquid turbine performance and flow behavior, in: Proc. ASME Turbo Expo 2008 Power Land, Sea, Air. Vol. 6 Turbomachinery, Parts A, B, C, Berlin, Germany, 2008: pp. 2287–2295. https://doi.org/10.1115/GT2008-50391.

[31] K. Li, J. Sun, J. Fu, P. Song, Design and numerical flow analysis of a LNG power recovery turbine, in: Proc. ASME Turbo Expo 2013 Turbine Tech. Conf. Expo. Vol. 5B Oil Gas Appl. Steam Turbines, San Antonio, Texas, USA, 2013. https://doi.org/10.1115/GT2013-94900.

[32] Z. He, Y. Ge, J. Sun, K. Wang, Numerical study of cavitating behavior in a cryogenic liquid turbine, in: Proc. ASME Turbo Expo 2012 Turbine Tech. Conf. Expo. Vol. 8 Turbomachinery, Parts A, B, C, Copenhagen, Denmark, 2012: pp. 2581–2592. https://doi.org/10.1115/GT2012-68774.

[33] P.J. Zwart, A.G. Gerber, T. Belamri, A two-phase flow model for predicting cavitation dynamics, in: ICMF 2004 Int. Conf. Multiph. Flow, Yokohama, Japan, 2004.

[34] P. Song, J. Sun, K. Wang, Z. He, Development of an optimization design method for turbomachinery by incorporating the cooperative coevolution genetic algorithm and adaptive approximate model, in: Proc. ASME 2011 Turbo Expo Turbine Tech. Conf. Expo. Vol. 7 Turbomachinery, Parts A, B, C, Vancouver, British Columbia, Canada, 2011: pp. 1139–1153. https://doi.org/10.1115/GT2011-45411.

[35] P. Song, J. Sun, K. Wang, Swirling and cavitating flow suppression in a cryogenic liquid

turbine expander through geometric optimization, Proc. Inst. Mech. Eng. Part A J. Power Energy. 229 (2015) 628–646. https://doi.org/10.1177/0957650915589062.

[36]   P. Song, J. Sun, C. Huo, Enhancing refrigeration capacity of turbo expander by means of multipoint design optimization, Int. J. Refrig. 108 (2019) 60–78. https://doi.org/10.1016/j.ijrefrig.2019.08.035.

[37]   P. Song, J. Sun, C. Huo, Cavitating flow suppression for a two-phase liquefied natural gas expander through collaborative fine-turning design optimization of impeller and exducer geometric shape, J. Fluids Eng. 142 (2020) 051401. https://doi.org/10.1115/1.4045713.

[38]   P. Song, J. Sun, Cryogenic cavitation mitigation in a liquid turbine expander of an air-separation unit through collaborative fine-tuned optimization of impeller and fairing cone geometries, Energies. 13 (2020) 50. https://doi.org/10.3390/en13010050.

[39]   K. Wang, J. Sun, P. Song, C. Huo, Influence of impeller fairing cone geometry on cavitating flow behavior in a cryogenic liquid turbine expander, in: Proc. ASME Turbo Expo 2016 Turbomach. Tech. Conf. Expo. Vol. 9 Oil Gas Appl. Supercrit. CO2 Power Cycles; Wind Energy, Seoul, South Korea, 2016: p. V009T24A011. https://doi.org/10.1115/GT2016-56778.

[40]   H. Li, W. Li, X. Zhang, Y. Zhu, Z. Zuo, H. Chen, Design method of a two-phase annular nozzle in cryogenic liquid expander, Proc. Inst. Mech. Eng. Part A J. Power Energy. 233 (2019) 762–772. https://doi.org/10.1177/0957650918822943.

[41]   H. Li, Z. Shao, X. Zhang, Y. Zhu, W. Li, H. Chen, Z. Yu, Preliminary design and performance analysis of the liquid turbine for supercritical compressed air energy storage systems, Appl. Therm. Eng. 203 (2022) 117891. https://doi.org/10.1016/j.applthermaleng.2021.117891.

[42]   Y. Ren, J. Sun, R. Zheng, P. Song, K. Wang, Investigation of impeller strength for a cryogenic liquid turbine, in: Proc. ASME Turbo Expo 2010 Power Land, Sea, Air. Vol. 6 Struct. Dyn. Parts A B, Glasgow, UK, 2010: pp. 1333–1343. https://doi.org/10.1115/GT2010-23125.

[43]   K. Wang, J. Sun, Z. He, P. Song, Prediction of axial thrust load acting on a cryogenic liquid turbine impeller, in: Proc. ASME 2011 Turbo Expo Turbine Tech. Conf. Expo. Vol. 6 Struct. Dyn. Parts A B, Vancouver, British Columbia, Canada, 2011: pp. 487–498. https://doi.org/10.1115/GT2011-45273.

[44]   N. Yuan, J. Sun, P. Song, C. Huo, S. Sun, Investigation of flow-induced radial force and its influence on rotor dynamics for a cryogenic liquid turbine expander, in: Proc. ASME Turbo Expo 2018 Turbomach. Tech. Conf. Expo. Vol. 7A Struct. Dyn., Oslo, Norway, 2018: p. V07AT33A011. https://doi.org/10.1115/GT2018-75443.

[45]   S. Rane, L. He, Modelling of flash boiling in two phase geothermal turbine, in: Proc. 16th UK Heat Transf. Conf., Nottingham, United Kindom, 2019: p. 005.

[46]   S. Rane, L. He, Two-Phase Flow Analysis and Design of Geothermal Energy Turbine, in: IOP Conf. Ser. Mater. Sci. Eng., IOP Publishing, 2019: p. 12043.

[47]   S. Rane, L. He, CFD analysis of flashing flow in two-phase geothermal turbine design, J. Comput. Des. Eng. 7 (2020) 238–250. https://doi.org/10.1093/jcde/qwaa020.

[48]   S. Rane, L. He, Numerical analysis of a novel two-phase turbine using thermal non-Equilibrium, homogeneous nucleation phase change, Therm. Sci. Eng. Prog. 22 (2021) 100827. https://doi.org/10.1016/j.tsep.2020.100827.

[49]   H. Moustapha, M.F. Zelesky, N.C. Balnes, D. Japikse, Axial and radial turbines, Concepts NREC, Vermont, US, 2003.

[50]   S.L. Dixon, C. Hall, Fluid mechanics and thermodynamics of turbomachinery, Butterworth-

Heinemann, 2014. https://doi.org/10.1016/C2011-0-05059-7.

[51]   J.D. Denton, Loss mechanisms in turbomachines, in: Proc. ASME 1993 Int. Gas Turbine
       Aeroengine Congr. Expo. Vol. 2 Combust. Fuels; Oil Gas; IGTI Sch. Award Appl. Cycle
       Innov. Heat Transf. Electr. Power; Ind. Cogener. Cer, Cincinnati, Ohio, USA, 1993: p.
       V002T14A001. https://doi.org/10.1115/93-GT-435.

[52]   A. Yu, Y. Tang, Q. Tang, J. Cai, L. Zhao, X. Ge, Energy analysis of Francis turbine for various
       mass flow rate conditions based on entropy production theory, Renew. Energy. 183 (2022)
       447–458. https://doi.org/10.1016/j.renene.2021.10.094.

Highlights

1. Geometrical models of liquid turbines affect the accuracy of predicted efficiency.

2. The model with a nozzle and a rotor predictes the efficiency with 15.8% error.

3. The total pressure loss of the rotor accounts for the largest portion among all parts.

4. The nonuniform flow in the nozzle and the rotor is significant at low flow rates.